THz Channel Characterization of Chip-to-Chip Communication in Desktop Size Metal Enclosure

Jinbang Fu, Prateek Juyal, and Alenka Zajić, *Senior Member, IEEE*

***Abstract*— This article presents characterization of terahertz (THz) wireless channel inside a desktop size metal enclosure with the consideration of several different scenarios. Measurements indicate that both traveling wave and resonating modes exist inside the metal enclosure. Measurements for line-of-sight (LoS) propagation inside the empty metal enclosure show that the path loss significantly changes as a function of the transceiver's height. It is found that this variation is due the resonant modes, contribution to the received power. Reflected-non-LoS (RNLoS) measurements show that for the same distance, the difference between the mean path loss measured inside the metal box and in a free space is limited to 1 dB, with traveling wave dominating the channel. This indicates that reflectors can be used as wave-guiding objects in metal enclosures. Finally, obstructed-LoS (OLoS) path loss measurements with the parallel dual in-line memory modules (DIMMs) as obstructions show the constructive/destructive effect on the waves due to multipath introduced by the parallel-plate structures. Compared to the free space scenarios, multipath is introduced by the traveling wave bouncing back and forth between the transceiver sides of the cavity, which introduces stronger fluctuations in observed pathloss and reduces the coherence bandwidth of the channel.**

***Index Terms*— Channel characterization, channel measurements, channel modeling, channel sounding, chip-to-chip wireless channels, terahertz (THz) communications.**

I. Introduction

WIRELESS communications have been proposed as a future solution for the chip-to-chip communication inside a desktop [1]. Wireless communications have potential for reducing the assembly cost of chips and the complexity of system design and maintenance [1]–[15]. One limitation of current wireless communication systems is its transmitting data rate. Currently used wired communication systems have data rate close to 100, 200, or 600 Gb/s through the InfiniBand high data rate 2×, 4×, or 12× link, respectively, and these data rates are expected to double through InfiniBand next data rate links by 2020 [16]. However, current wireless communication systems can only achieve 10 Gb/s at 5 GHz frequency band with the new IEEE802.11ax standard, MIMO-orthogonal frequency-division multiplexing modulation, and complicate coding [17]. Although, with the incoming standard IEEE802.11ay, the peak transmitting data rate is expected to improve to 20 Gb/s at 60 GHz frequency band in 2019 [18], it is still low to be useful for chip-to-chip communications. To address this problem, terahertz (THz) wireless communications have been proposed for its larger bandwidth and requiring smaller antenna footprints [1], [12], [19]–[26].

Channel characterization is the first necessary step to design THz chip-to-chip wireless communication systems inside a desktop. In the microwave frequency range, 3.1–10 GHz, measurements for board-to-board communications have been conducted inside two desktops, one with crowded interior and the other one with relative empty interior [10]. Also, the chip-to-chip communication has been characterized in both closed and open computer cases in the similar frequency band [11]. At THz frequencies, indoor communication has been conducted for line-of-sight (LoS) propagation by varying distance between transmitter (Tx) and receiver (Rx), and for non-LoS (NLoS) propagation with different transmitting and receiving angles, shadowing effect, and reflection and diffraction from various materials [1], [27]–[31]. For waveguide structures with different dimensions, measurements have been done at both 60 and 300 GHz for intradevice communication, also the channel model based on ray tracing has been proposed [32]. Finally, on-board THz wireless communication measurements have been conducted by considering different possible scenarios like LoS, reflected-NLoS (RNLoS), obstructed-LoS (OLoS), and NLoS [1]. However, no channel measurements have been performed at 300 GHz that characterize propagation in metal enclosures such as computer desktops. Hence, this article shows the characterization of 300 GHz wireless channel inside a desktop size metal box. Some early investigations have been reported in [33].

Measurements have been conducted with the consideration of different scenarios: LoS propagation inside a desktop size metal box, RNLoS with and without dual in-line memory module (DIMM) as the reflecting surface, OLoS with a parallel-plate structure as an obstruction, NLoS with heat sink as an obstruction, and LoS over a field programmable gate array (FPGA) board. The contributions of this article are as follows.

1) Measured path loss inside the desktop size metal box: It was observed that path loss varies with respect to transceiver's height, h, which is due to the effect of

Manuscript received November 24, 2018; revised May 15, 2019; accepted July 14, 2019. Date of publication August 19, 2019; date of current version November 27, 2019. This work was supported by the NSF CAREER ECCS Grant under Grant 1651273. The views and findings in this article are those of the authors and do not necessarily reflect the views of NSF. *(Corresponding author: Prateek Juyal.)*

The authors are with the School of Electrical and Computer Engineering, Georgia Institute of Technology College of Engineering, Atlanta, GA 30332 USA (e-mail: pjuyal3@gatech.edu).

Color versions of one or more of the figures in this article are available online at http://ieeexplore.ieee.org.

Digital Object Identifier 10.1109/TAP.2019.2934908

resonating modes, contribution to the received power. Also, it is found that the parallel-plate structure constructed by two DIMMs with distance ($\omega \leq 40\lambda$) in between always have constructive effect to the channel; however, this constructive effect can be negligible when $\omega \geq 60\lambda$.

2) Compared measurements inside the box with the measurements performed in free space: It was found that path loss measured inside the metal box has more fluctuation over the observed frequency band, which is due to the resonating modes combined with reflections of traveling waves inside the cavity. Additionally, measurements show that resonating modes have constructive effect to the channel as the mean path loss measured inside the metal box is always lower or equal to the mean path losses measured in the free space.
3) Proposed path loss model for inside the box metal propagation: The LoS path loss inside an empty metal cavity can be defined as a combination of the mean path loss of traveling wave and the received power variation due to resonant modes.
4) Analyzed power delay profiles (PDPs), the mean excess delay τ_m, rms delay spread τ_{rms}, and coherence bandwidth B_c: The results indicate that multipath is introduced by signal bouncing back and forth between the transceiver sides of the cavity, which reduces the coherence bandwidth of the channel. Also, the results indicate that for NLoS link with heat sink as an obstruction, signal also bounces of the side walls inside the box and the heat sink.

The remainder of this article is organized as follows. Section II briefly describes measurement equipment and setup, while Section III describes measurement scenarios. Section IV presents the measured results, path loss, and channel modeling and discusses the findings. Section V provides concluding remarks.

II. Measurement Setup

This measurement setup includes the N5224A PNA vector network analyzer (VNA), the Virginia Diodes, Inc. (VDI) transmitter (Tx210), and the VDI receiver (Rx148). The VNA provides the input signal with the range of 10 MHz to 20 GHz. The VDI transmitter amplifies and converts the signal to 300 GHz. The THz signal is transmitted by the diagonal horn antenna in the range of 280–320 GHz. At the receiver side, the VDI receiver downconverts the received signal to an intermediate frequency (IF) of 9.6 GHz. The VNA records the upper side of down converted signal in the range of 9.6–29.6 GHz. Fig. 1 shows the block diagram of the measurement system, and Table I summarizes all measurement parameters.

The antenna used in this measurement is a pyramidal horn antenna whose gain varies in the range of 22–23 dBi over the frequency band of observation which is 300–312 GHz. The theoretical half power beamwidths are about 12° in azimuth and elevation. The physical dimension of the horn aperture is 9.15 mm, which limits the far-field boundary to be 16.7 cm at 300 GHz.

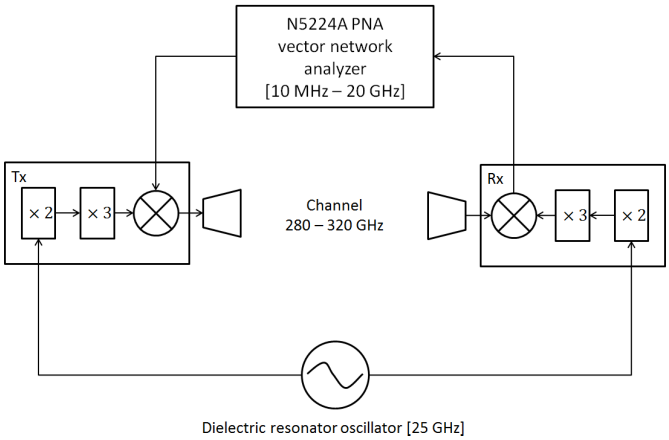

Fig. 1. Geometry-based statistical model of chip-to-chip communications in metal enclosures loaded with scatterers.

TABLE I
Measurement Parameters

Parameter	Symbol	Value
Measurement points	N	801
Intermediate frequency bandwidth	Δf_{IF}	20 kHz
Average noise floor	P_{N}	-90 dBm
Input signal power	P_{in}	0 dBm
Start frequency	f_{start}	10 MHz
Stop frequency	f_{stop}	20 GHz
Bandwidth	B	19.99 GHz
Time domain resolution	Δt	0.067 ns
Maximum excess delay	τ_{m}	40 ns

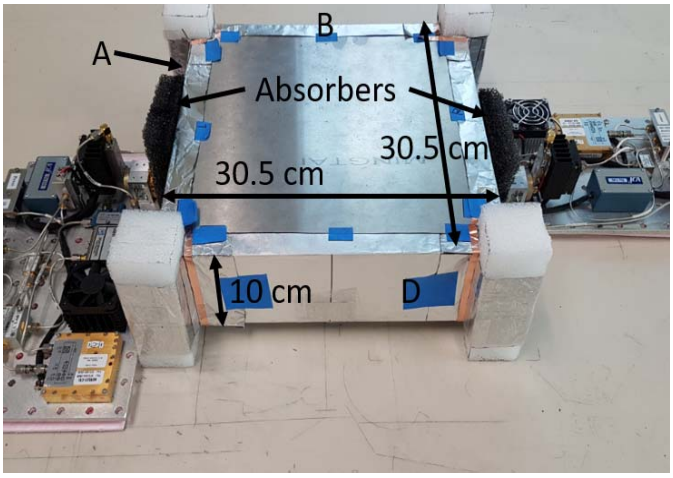

Fig. 2. LoS measurement scenario in an empty metal box.

III. Measurement Scenarios

A. LoS Inside a Computer Desktop Size Metal Box

To develop THz wireless communication schemes for chip-to-chip communications, the first step is to understand its propagation mechanisms inside an empty metal box. An aluminum box was fabricated with the size of 30.5 cm × 30.5 cm × 9.6 cm, which approximates computer desktop casing, as shown in Fig. 2. Two square aluminum

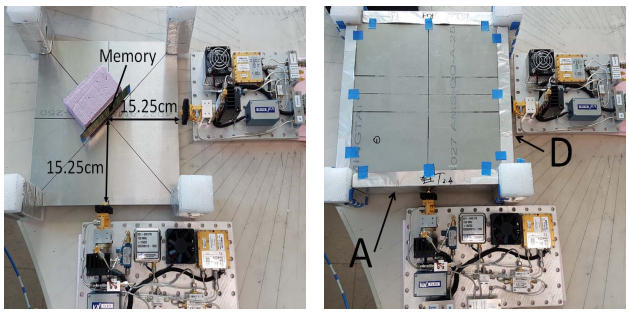

(a) (b)

Fig. 3. RNLoS measurement setups for (a) free space and (b) in-box measurements with/without DIMM as the reflecting surface.

plates with the length of 30.5 cm were fixed by foams at four corners to form as the top and bottom wall of the metal box. The other four sides of the metal box were wrapped by aluminum foils. These side walls are labeled as A, B, C, and D. Box was sandwiched by Tx and Rx with antennas aligned horizontally. Based on the antennas' heights for both Tx and Rx, h, two diagonal openings with the horn antenna's size were drilled on the transceiver sides (sides A and C) of the metal box. The distance from the center of antennas to side B/side D of the metal box is equal to half of its width. To characterize the resonating modes inside the metal box, measurements have been performed with h varied from 0 to 6.6 cm with the step size of 0.6 cm. The parameter h here refers to the distance from the bottom edge of the horn to the ground of the metal box. The distance between phase center and bottom edge of the horn antenna is 4.575 mm. Absorbers were utilized to eliminate reflections from the backside of antennas as shown in Fig. 2.

B. RNLoS With and Without Memory Card as the Reflecting Surface

DIMM are typically vertically plugged and connected to the motherboard of a desktop. To investigate whether DIMM can be used as a reflector to establish a wireless link when Tx and Rx are positioned orthogonal to each other, measurements have been performed both in free space and inside the metal box, with DIMM diagonally aligned with the transceiver as shown in Fig. 3. The Tx and Rx are positioned on the sides A and D, respectively, as shown in Fig. 3. For the box measurements, two diagonal openings were drilled on sides A and D of the box for the horn antennas. Both flat side and component side of the DIMM were measured with $h = 2.4$ cm. The scenario without DIMM between transceivers also has been measured.

C. OLoS Link With Parallel-Plate Structure as an Obstruction

One possible scenario for the on-board chip-to-chip wireless communication in a desktop is the LoS link being influenced by parallel-plate structures, like the DIMMs being connected in parallel on the motherboard. Measurements were performed to explore whether these DIMMs can be utilized to improve the wireless communication by introducing multipath.

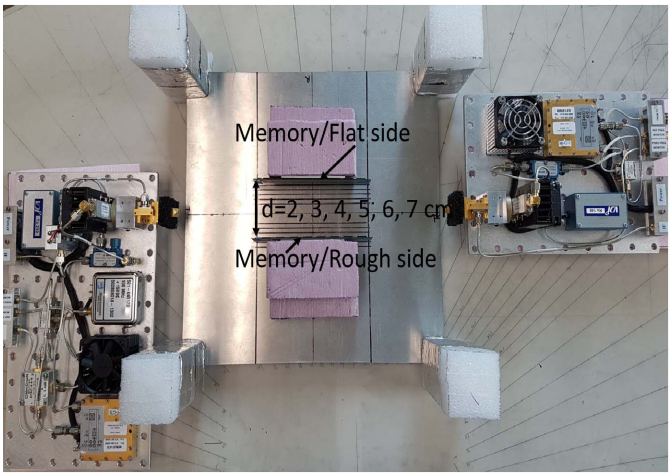

Fig. 4. Setup for the OLoS measurement.

Fig. 5. NLoS with heat sink as an obstruction.

Fig. 4 shows the setup for the measurements. Height, h, is the same as the setup for Section III-B. Two DIMMs were placed in parallel in the middle of the bottom wall. Also, the distance between these two DIMMs, d, has been varied from 2 to 7 cm with the step size of 1 cm to investigate the relationship between this distance and the path loss. For comparisons, measurements have been performed both in free space and inside the metal box.

D. NLoS With Heat Sink as an Obstruction

On the crowded motherboard, LoS link is not always possible due to obstructions created by various components on the motherboard. Therefore, we did many measurements to test the feasibility of the RNLoS and OLoS link. However, there are components like the heat sink which have openings so that the signal can go through them to the receiver. In this experiment, measurements have been performed to test the influence of the heat sink. Fig. 5 shows the measurement setup. As shown in the Fig. 5, the heat sink with the size of 7.8 cm $\times$ 6.35 cm $\times$ 6.8 cm was put in the center of the box. The distance from the Tx to one end of the heat sink (also the distance from the Rx to another end of the heat sink) is equal to 12.6 cm. To fully understand the impact of the fins of

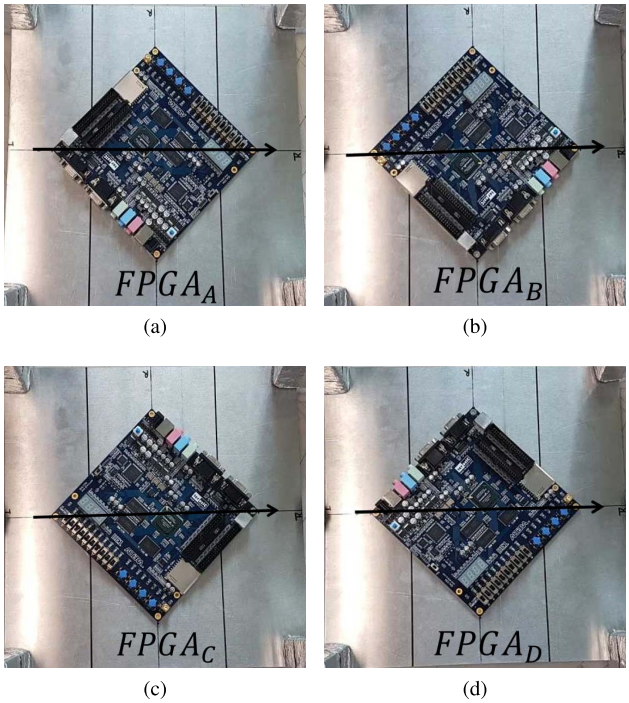

Fig. 6. LoS over an FPGA board with measurement scenarios of (a) $FPGA_A$, (b) $FPGA_B$, (c) $FPGA_C$, and (d) $FPGA_D$.

the heat sink on the wireless link, several measurements have been performed by moving the heat sink toward the right side (side D) of the box with the step size of 2.5 mm. The height of the antenna was set to 2.4 cm over the bottom of the box, which is the same as the setup for previous measurements. To show the comparison, measurements have been performed both in free space and inside the metal box.

E. LoS Over an FPGA Board

For the on-board chip-to-chip THz wireless communication, it is necessary to consider the influence of the printed circuit board (PCB) with components integrated on it. An FPGA board with its length and width of 15.2 cm and the maximum height of 1.5 cm was put on the center of the bottom plate to let the EM wave travel through the FPGA's diagonals. By counterclockwise turning the FPGA board every 90°, we did four measurements which are $FPGA_A$, $FPGA_B$, $FPGA_C$, and $FPGA_D$, as shown in Fig. 6. With a height, h, of 2.4 cm, measurements have been performed in both free space and the metal box. Please note that, at 2.4 cm, antennas are high enough to avoid the obstruction of big components like the power port and the video graphics array port on the board, but at this height, those big components may still be able to affect the traveling wave. To show this, another measurement has been done inside the box with the height, h, of 4.8 cm at which those big components have little effect on the traveling wave.

IV. Measurement Results and Analysis

A. Path Loss and Multipath Characterization

This section analyzes and discusses the results of the measurements described in Section III. Here, PL is used to represent the measured path loss and is defined as

$$PL = \frac{P_t G_t G_r}{P_r} \tag{1}$$

where P_t represents the transmit power, G_t and G_r are the transmit and receive gain of the antenna being used, respectively, and P_r is the received power. The measured path loss was compared with the theoretical free-space path loss $\tilde{PL}$ defined as [34]

$$\tilde{PL} = \left(\frac{4\pi d}{\lambda}\right)^2 \tag{2}$$

where d represents the signal traveling distance, and λ is the wavelength in free space.

For the measurements performed inside the metal box, which acts as a cavity resonator, resonant modes should be taken into consideration. Fig. 7 shows the geometry of the metallic cavity with diagonal openings. The transverse components of the electric field ($E_z = 0$) of TE mode inside the cavity can be written as [35]

$$E_y = \frac{j\omega_{mnp}\mu k_x H_0}{k_{mnp}^2 - k_z^2} \sin\frac{m\pi x}{a} \cos\frac{n\pi y}{b} \sin\frac{p\pi z}{z} \tag{3}$$

$$E_x = -\frac{j\omega_{mnp}\mu k_y H_0}{k_{mnp}^2 - k_z^2} \cos\frac{m\pi x}{a} \sin\frac{n\pi y}{b} \sin\frac{p\pi z}{z} \tag{4}$$

where H_0 is an arbitrary constant with units of ampere per meter and m, n, and p are integers. The eigenvalues k_{mnp} satisfy

$$k_{mnp}^2 = \left(\frac{m\pi}{a}\right)^2 + \left(\frac{n\pi}{b}\right)^2 + \left(\frac{p\pi}{c}\right)^2 = k_x^2 + k_y^2 + k_z^2 \tag{5}$$

where

$$k_x = \frac{m\pi}{a}, \quad k_y = \frac{n\pi}{b}, \quad k_z = \frac{p\pi}{c} \tag{6}$$

where a, b, and c in these equations represent the height, length, and width of the cavity, respectively. The resonant frequencies f_{mnp} can be determined as

$$f_{mnp} = \frac{1}{2\sqrt{\mu\epsilon}} \sqrt{\left(\frac{m}{a}\right)^2 + \left(\frac{n}{b}\right)^2 + \left(\frac{p}{c}\right)^2}. \tag{7}$$

The impulse response for the time-invariant channel can be written as [36]

$$h(\tau, d) = \sum_{k=1}^{L} a_k(d) exp(j\theta_k(d))\delta(\tau - \tau_k) \tag{8}$$

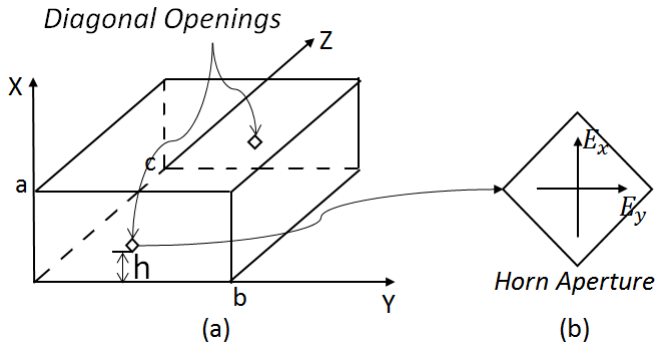

Fig. 7. (a) Rectangular metal cavity with diagonal openings and (b) horn antenna aperture.

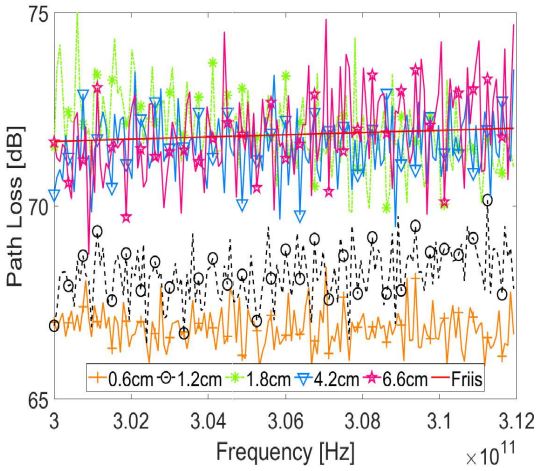

Fig. 8. Measured and calculated path loss variation in frequency for LoS in a metal box as a function of the antenna's height, h.

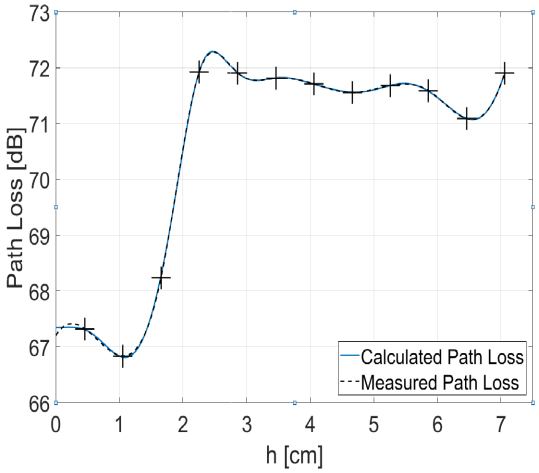

Fig. 9. Measured and calculated mean path loss as a function of h.

where d represents the signal traveling distance, L represents the number of multipath components, a_k represents the amplitude of the kth multipath component, θ_k is the associated phase, and τ_k represents the excess delay of the kth path compared with the first one, and $\delta(\cdot)$ is the Dirac delta function. The equations for the mean excess delay, τ_m, the rms delay spread, τ_{rms}, and the coherence bandwidth, B_c, of the channel can be written as [36]

$$\tau_m = \sum_{k=1}^{L} \tau_k \cdot |h(t, \tau_k, d)|^2 \tag{9}$$

$$\tau_{rms} = \sqrt{\sum_{k=1}^{L} (\tau_k - \tau_m)^2 |h(t, \tau_k, d)|^2} \tag{10}$$

$$B_c = \frac{1}{2\pi \tau_{rms}} \tag{11}$$

where L is the number of multipath components, and τ_k represents excess delay of the kth path.

B. Characterization of LoS Propagation Inside a Metal Box

Fig. 2 describes the measurement scenario for exploring the signal propagation mechanisms inside an empty metal box. Fig. 8 shows the measured path losses for in the box measurements and compares them with the theoretical path loss calculated using Friis formula. For the measurements with $h < 1.8$ cm, path losses are lower than Friis formula prediction, while for $h > 1.8$ cm, path losses are aligned with the Friis formula prediction. This variation in path losses can be explained by observing that different resonating modes contribute to the received power. We note here that since transmit power is kept constant, the variation in the path loss is equal to the variation of the received power. Therefore, the path loss of LoS propagation inside the metal box can be considered as the combination of the path loss of traveling wave and the received power variation due to the resonating modes. Fig. 9 compares the measured and theoretically calculated mean path loss with respect to height, h. The mean of measured path loss at certain height, h, is calculated by averaging the continuous wave, as shown in Fig. 8, over all recorded frequencies. The measured path loss curve shown in Fig. 9 is the interpolation of these averaged points which are also marked on the curve.

The theoretical path loss $(PL^T)_{\text{dB}}$ in Fig. 9 is calculated as

$$(PL^T)_{\text{dB}} = \overline{(\tilde{PL})}_{\text{dB}} + 10\log_{10}(|E|^2)^{-1} \tag{12}$$

where $\overline{\tilde{PL}}$ represents the mean path loss of traveling wave and can be calculated by averaging Friis formula (2) over the frequency band as

$$\overline{\tilde{PL}} = \frac{1}{\Delta f} \int_{\Delta f} \tilde{PL} df. \tag{13}$$

In this situation, $d = D = 30.5$ cm, which is the length of the box. Component $10\log_{10}(|E|^2)^{-1}$ represents the received power variation contributed by resonating modes. $|E|^2$ can be written as

$$|E|^2 = |E_x|^2 + |E_y|^2 = \left| \sum_{m=1}^{M} E_{ym} \right|^2 + \left| \sum_{m=1}^{N} E_{xm} \right|^2 \tag{14}$$

where E_{ym} and E_{xm} are given by (3) and (4), respectively. For h variation in the x-direction, (3) and (4) can be simplified as follows:

$$E_{ym} = A_m \sin \frac{m\pi x}{a} \tag{15}$$

$$E_{xm} = B_m \cos \frac{m\pi x}{a}. \tag{16}$$

Using curve fitting, we have found that the first eight modes of the TE mode dominate the resonant cavity in the box and the coefficients of these modes are empirically found to be $A_1 = 0.441$, $B_1 = -0.173$, $A_2 = -0.583$, $B_2 = 0.060$, $A_3 = 0.757$, $B_3 = -0.056$, $A_4 = -0.254$, $B_4 = 0.352$, $A_5 = 0.274$, $B_5 = -0.113$, $A_6 = 0.128$, $B_6 = 0.394$, $A_7 = 0.968$, $B_7 = 0.892$, $A_8 = 0.269$, and $B_8 = 0.323$.

Fig. 10 presents the PDP of the empty box measurements for different h values. After the first arriving peak, there are several clusters of peaks that arrive with delay of 2.05 ns. This delay is due to the signal traveling on a certain path

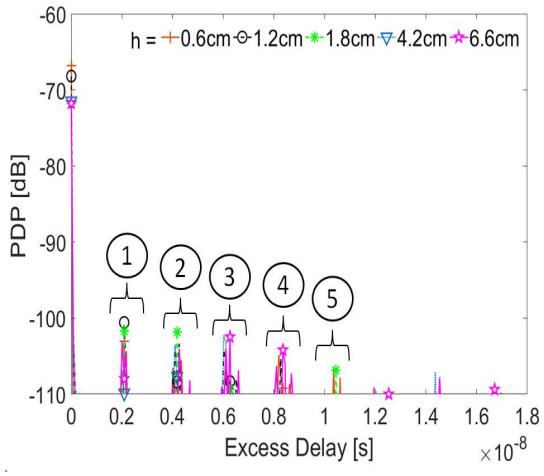

Fig. 10. PDP of the metal box measurements shown in the Fig. 1 as a function of antenna height h.

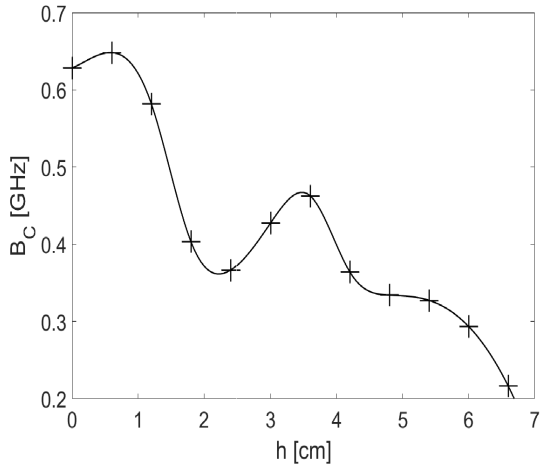

Fig. 11. Coherence bandwidth, B_c, as a function of antenna height h, for the channel inside a metal box.

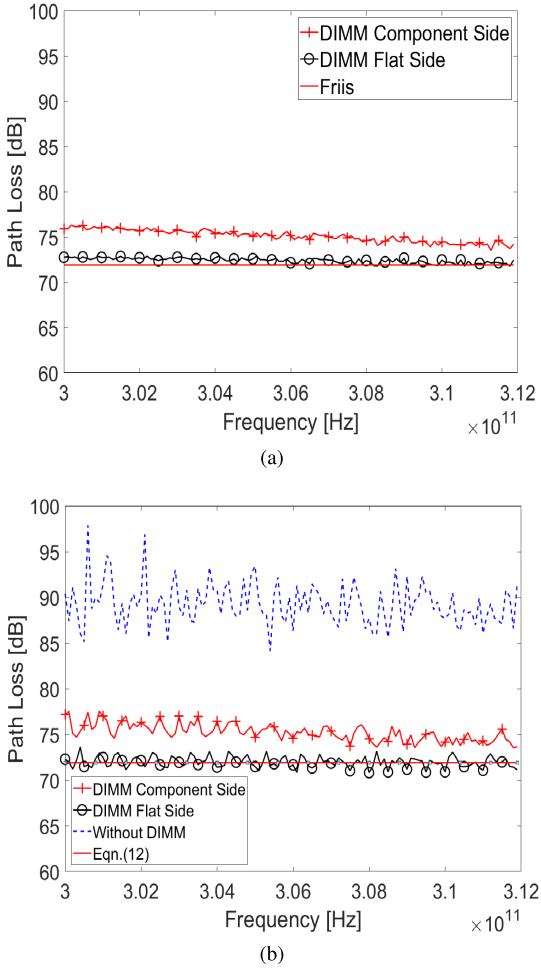

Fig. 12. Measured and calculated path losses of RNLoS with rough DIMM side, flat DIMM side, and without DIMM as the reflecting surface for the measurements (a) in free space and (b) inside the box.

many times and the path difference between any two close paths can be calculated as

$$T \times c = 2.05 \times 10^{-9} \cdot 3 \times 10^{8} = 61.5 \text{ cm} \qquad (17)$$

which is close to twice of the box's length. Therefore, it can be concluded that the signal bounces several rounds between the transceiver sides (sides A and C) of the box. This is due to the traveling wave inside the box.

Fig. 11 shows the coherence bandwidth B_c as a function of the antenna height h. Due to the traveling wave bouncing back and forth between the transceiver sides of the box, the B_cs of channel inside the empty box is below 1 GHz. This is due to the introduced multipath. It can be observed from Fig. 11 that the B_c has larger values closer to the bottom wall as compared to the antenna height $h > 4$ cm.

C. Characterization of RNLoS Inside a Metal Box

Fig. 12 compares the path losses of RNLoS link measured both in free space and inside the box. Measurement setup is shown in Fig. 4. Measured path losses are shown when DIMM component and flat side are used as reflecting surfaces. For comparison, we also plot the path loss for the scenario without DIMM between the transceivers. Fig. 12(a) compares the path loss measured in free space with Friis formula. Due to the reflection losses, the path losses for both flat and rough side of the DIMM are greater than the Friis formula prediction. The path loss of the rough side of DIMM is greater than the path loss of the flat side of DIMM, which is expected as the rough DIMM side is more rugged than the flat side of DIMM. In case of the scenario without DIMM between transceivers, the measured pathloss is near noise floor which indicates no communication between Tx and Rx. This is also observed in [28]. Fig. 12(b) shows the measurements inside the metal box. It is found that for both rough and flat side of the DIMM as the reflecting surfaces, the path loss measured in the metal box is at the similar level of the path loss measured in the free space with the differences of the mean path loss limited to 1 dB. However, it is interesting to notice that curves shown in Fig. 12(b) have stronger ripples than curves in Fig. 12(a). This is due to the effect of resonating modes and reflections of traveling wave in the metal box. Furthermore, the path loss for the measurement without DIMM between the transceivers is shown in Fig. 12(b). In contrast to the free space, this

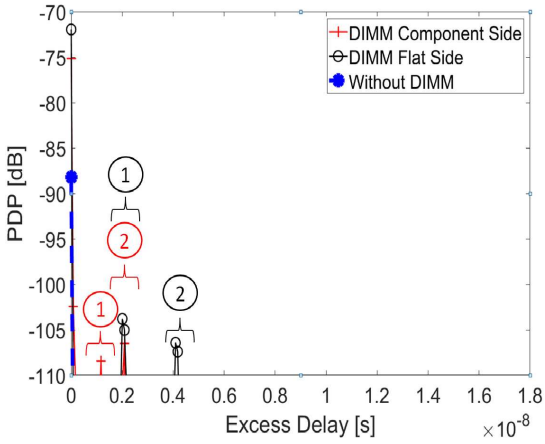

Fig. 13. PDP of RNLoS link with rough side DIMM, flat side DIMM, and without DIMM as the reflecting surface for in-box measurements.

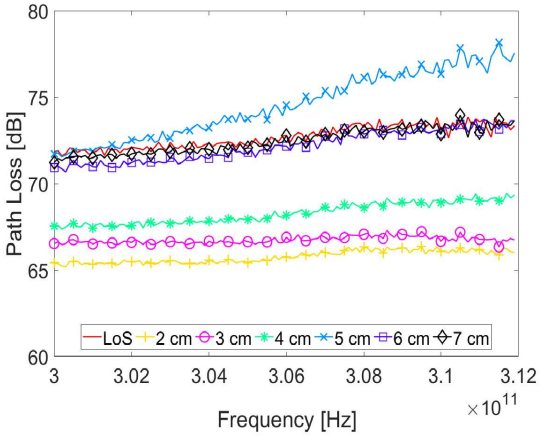

Fig. 14. Path loss of LoS and OLoS links measured in free space.

TABLE II

τ_m, τ_{rms}, AND B_c OF RNLoS LINK FOR MEASUREMENTS INSIDE THE BOX

Measurements	τ_m (ps)	τ_{rms} (ns)	B_c (GHz)
DIMM Flat Side	4.971	0.1251	1.273
DIMM Component Side	2.217	0.0618	2.576
Without DIMM	-	-	-

path loss is not close to the noise floor and is due to the resonating modes that exist in the box. This also demonstrates that the channel inside the cavity is dominated by the traveling wave.

Fig. 13 shows the PDPs of the RNLoS link for the in-box measurements. From the PDP plot, it can be observed that there are two later arriving peaks that are result of reflections from both rough and flat DIMM side. For the flat side of DIMM, those two later arriving peaks are located at 2.05 and 4.09 ns. These two later arriving peaks illustrate that with the help of the DIMM, the signal can travel several rounds between the transceiver sides (sides A and D) of the box. For the rough DIMM side, those two later arriving peaks are at 1.17 and 2.05 ns. This shows that signal also bounced back and forth between the DIMM and the transceiver.

Table II shows τ_m, τ_{rms}, and B_c of the RNLoS link for the measurements performed inside the box. When comparing with the PDP plot of the empty box measurements, the in-box RNLoS link has less later arriving peaks, which provides the channel a much wider coherence bandwidth. From Fig. 13, it can be observed that the later arriving peaks' amplitudes of the rough side DIMM are lower than the later arriving peaks' amplitudes of the flat side DIMM, which indicates that comparing with the DIMM flat side, the channel constructed with the rough side of DIMM as the reflecting surface can achieve a wider coherence bandwidth. Note that DIMM can be utilized to help construct the wireless link when the Tx and Rx are in perpendicular with each other.

D. Characterization of OLoS Link Through a Parallel-Plate Structure

To understand the propagation mechanisms of EM waves with the influence of parallel-plate structures, measurements

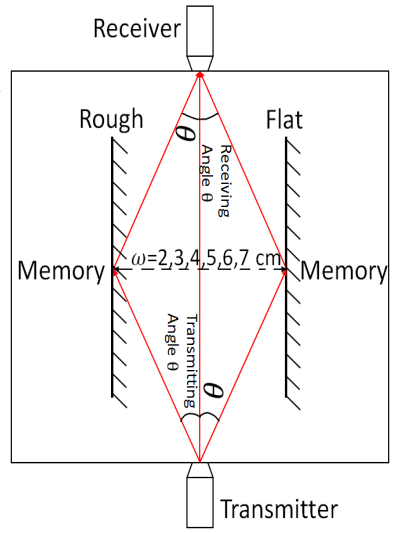

Fig. 15. Possible paths for OLoS link.

have been conducted with the measurement setup shown in Fig. 4. Fig. 14 compares the path loss curves for the measurements with and without parallel DIMMs as an obstruction. Measurements are performed for different ω as shown in Fig. 15. Fig. 14 shows that for $\omega \leq 4$ cm, path losses are lower than the path loss of LoS signal. It implies that the parallel-plate structure is constructive with small distance in between. Also, the constructive effect reflects that multipath exists when the distance between the parallel DIMMs is small. Based on the setup of the measurement, three possible paths have been observed as shown in Fig. 15. The first path is the LoS propagation for which the signal travels directly from the Tx to the Rx and the others are the signal travels to the Rx through the reflection on the DIMMs. It is observed that the path loss for the measurements of parallel DIMMs with the $\omega = 6, 7$ cm is aligned with the path loss of the LoS signal, which means that the effect of multipath propagation is negligible when ω is large, $\omega \geq 60\lambda$. It is also observed that the path loss for $\omega = 5$ cm is greater than the path loss of LoS signal, which is due to the phase cancellation.

For the same ω values, measurements have been conducted inside the metal box. Path loss curves are shown in Fig. 16.

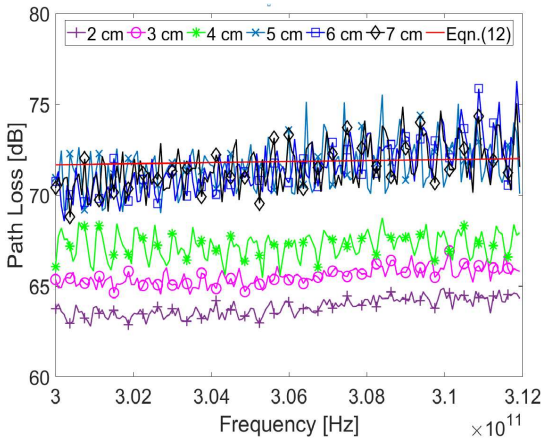

Fig. 16. Path loss of OLoS link measured in metal box.

TABLE III

MEAN PATH LOSS OF OLOS LINK MEASURED IN FREE SPACE AND INSIDE THE METAL BOX

ω (cm)	$\overline{PL}$ (Free Space) (dB)	$\overline{PL}$ (Metal Box) (cm)
2	65.76	63.80
3	66.74	65.51
4	68.26	67.21
5	74.34	71.49
6	72.12	71.42
7	72.44	71.48

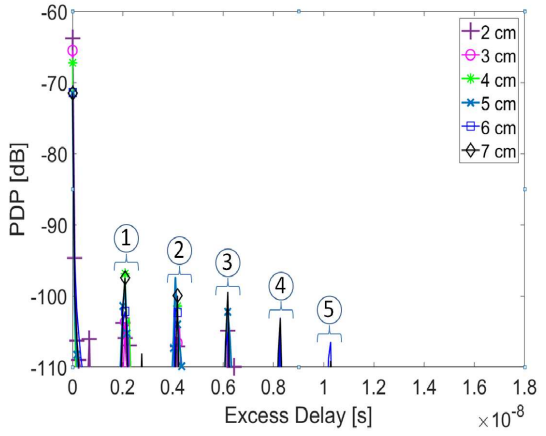

Fig. 17. PDP of OLoS link measured inside the metal box.

Table III compares the measured mean path losses $\overline{PL}$ for measurements in the free space and inside the metal box. Due to the effect of resonating modes, the channel inside the metal box has lower mean path loss and stronger path loss fluctuations over the frequency band as compared to the free space.

Fig. 17 shows the PDP plot of the OLoS link measured inside the metal box. It can be observed that there are five later arriving peaks. As what we showed in Section IV-B, these periodic later arriving peaks reflect the signal bouncing back and forth between the transceiver sides of the box. Table IV shows the mean excess delay, rms delay spread, and the coherence bandwidth of the OLoS link measured inside the metal box. For the ω equals 2, 3, and 4 cm between the DIMMs, the coherence bandwidths of the channel are in the level of GHz, while for ω equals 5, 6, and 7 cm between the DIMMs, the coherence bandwidths of the channel drop to 350 MHz, which again proved that for the parallel-plate structure with small spaces between plates, it is constructive to wireless link, and this constructive effect disappears when the distance between the DIMMs extends to a large value.

TABLE IV

MEAN EXCESS DELAY, RMS DELAY SPREAD, AND THE COHERENCE BANDWIDTH OF THE OLOS LINK MEASURED INSIDE THE METAL BOX

ω (cm)	τ_m (ps)	τ_{rms} (ns)	BC (GHz)
2	1.40	0.0759	2.0967
3	1.83	0.0803	1.9817
4	6.67	0.1396	1.1403
5	35.33	0.4007	0.3972
6	26.74	0.4010	0.3969
7	35.39	0.4394	0.3622

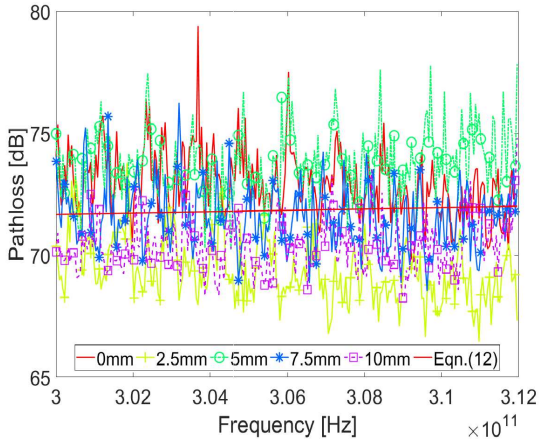

Fig. 18. Path loss of NLoS link measured inside the metal box.

E. Characterization of NLoS Link With Heat Sink as the Obstruction

To characterize the NLoS link with heat sink as the obstruction, measurements have been performed with the setups shown in Fig. 5. In the previous work [27], heat-sink-obstructed NLoS links were investigated in the free space environment. It was found that the measured mean path loss align with the Friis theoretical path loss for the various distances between the Tx and Rx. Also, it was shown that the heat sink provides the constructive/destructive interference between the LoS path and the other multipath. Here, we have investigated the heat-sink-obstructed NLoS links in the metallic enclosure environment setup, shown in the Fig. 18.

From Fig. 18, we can observe that the heat sink has either constructive or destructive effect on propagation. When the

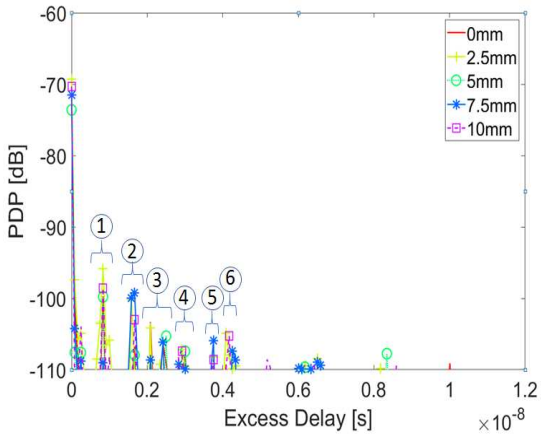

Fig. 19. PDP of NLoS link measured inside the metal box.

LoS path is clear, signal can arrive at the Rx through the gap between two fins of the heat sink, which can be considered as a parallel waveguide. Therefore, the mean path loss is lower than the Friis prediction. On the other hand, the heat sink has destructive effect on propagation when the LoS path is blocked by the fins of the heat sink for which the signal travels to the Rx via diffraction or multi-reflections. Also, it is observed in the measurements that the mean path loss values are lower than those in free space, which is due to the effect of resonating modes. Also, as compared to the free space measurements, the path loss measured inside the metal box has stronger ripples. It is observed that the maximum peak-to-peak variation is for $x = 0$ mm, which is 8.70 dB. These ripples are due to the effect of the resonating modes and the multipath introduced by the traveling wave. This can be supported by the PDP plot of the NLoS link inside the metal box presented in Fig. 19. It is observed that there are six clusters of later arriving peaks. The third cluster and the sixth cluster of peaks which are located at 2.085 and 4.087 ns respectively, as analyzed before, reflect the signal bouncing back and forth between the transceiver sides of the box. The first later arriving peak locates at 0.83 ns, which means that with this path, the signal travels $0.834 \times 10^{-9} \cdot 3 \times 10^{8} = 25.02$ cm more than the LoS propagation. Also, 25.02 cm is exactly the double of the distance from the Tx side of the cavity to one end of the heat sink, which means that the signal bounced a round between the side wall and the heat sink before traveling to the Rx. Therefore, it illustrates that besides bouncing back and forth between the transceiver sides of the box, signal also bounces around the transceiver side and the heat sink. This can also be supported by the second, fourth, and fifth clusters of later arriving peaks which are located at 1.67, 3, and 3.75 ns, respectively. Table V lists the excess mean delay, rms delay spread, and coherence bandwidth of the NLoS link measured inside the metal box. It can be seen that due to the multipath introduced by the traveling wave, the coherence bandwidths are narrow and in the range of 600–850 MHz.

F. Characterization of LoS Over an FPGA Board

To emulate the THz wireless communication in a real electronic device, measurements have been conducted with an FPGA board being fixed at the center of the bottom wall as shown in Fig. 6. Fig. 20(a) and (b) show the path losses for the measurements performed in free space and inside the metal box, respectively. It can be seen from Fig. 20(b) that the path loss for measurements performed inside the metal box is aligned with the calculated value from (12). The path losses for the measurements performed inside the metal box have much stronger ripples as compared to the free space measurements. It is observed that the maximum peak-to-peak variation is 6.73 and 1.60 dB in Fig. 20(a) and (b), respectively. This is because of the resonating modes

TABLE V
MEAN EXCESS DELAYS, RMS DELAY SPREADS, AND COHERENCE BANDWIDTHS FOR NLoS LINK WITH HEAT SINK AS THE OBSTRUCTION

Moving Distance (x) (mm)	τ_m (ps)	τ_{rms} (ns)	BC (GHz)
0	10.01	0.1988	0.8007
2.5	12.43	0.2551	0.6238
5	10.24	0.2144	0.7424
7.5	15.43	0.2394	0.6647
10	9.05	0.1916	0.8309

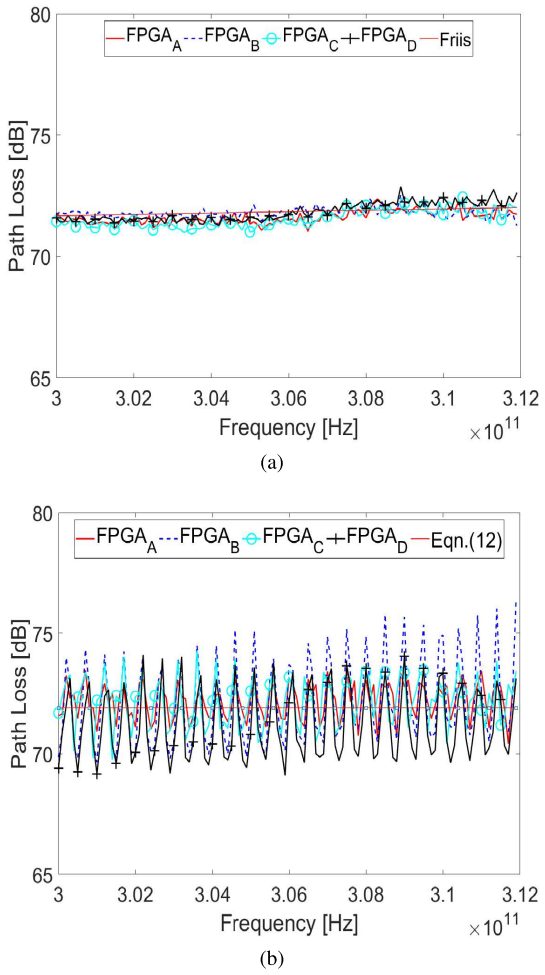

Fig. 20. Path losses of LoS over FPGA board measured (a) in free space and (b) inside the metal box.

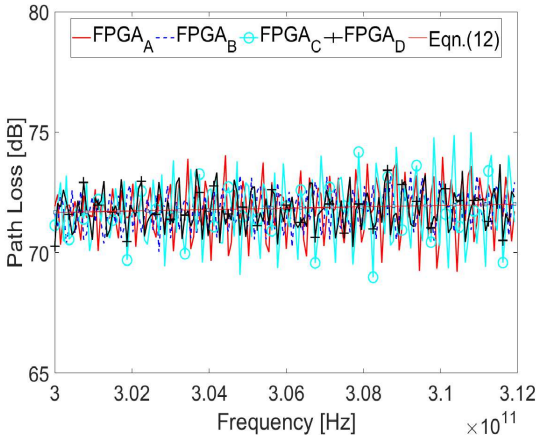

Fig. 21. Path loss for $h = 4.8$ cm.

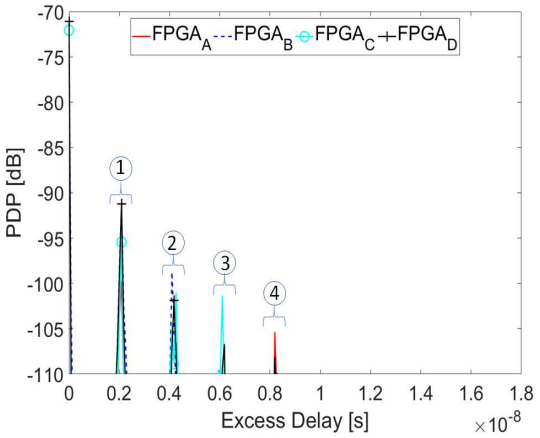

Fig. 22. PDP of LoS over FPGA board measured inside the metal box with h of 2.4 cm.

TABLE VI
MEAN EXCESS DELAYS, RMS DELAY SPREADS, AND COHERENCE BANDWIDTHS FOR THE MEASUREMENTS PERFORMED INSIDE THE METAL BOX WITH h OF 2.4 cm

Measurements	τ_m (ps)	τ_{rms} (ns)	B_c (GHz)
$FPGA_A$	14.10	0.2521	0.6314
$FPGA_B$	27.64	0.3282	0.4850
$FPGA_C$	33.98	0.3172	0.5017
$FPGA_D$	43.66	0.3441	0.4626

inside the box, signal bouncing back and forth between the transceiver sides of the box, and the reflection happened on the components of the FPGA board. To show this, measurements have been done for $h = 4.8$ cm. Fig. 21 shows the path loss for $h = 4.8$ cm. It is observed that peak-to-peak variation is 5.20 dB which is less than that for $h = 2.4$ cm, as shown in Fig. 20(b).

Fig. 22 shows the PDP plot of the in-box measurement. Later arriving peaks, once again, reflect the traveling wave bouncing back and forth between the transceiver sides of the box. Table VI lists the excess mean delay, rms delay spread, and the coherence bandwidth of the measurements performed inside the metal box with h of 2.4 cm. It can be observed from the table that due to the multipath introduced by the signal bouncing back and forth between the transceiver sides of the box, the coherence bandwidth of the channel is narrow and in the range of 480–640 MHz.

V. CONCLUSION

This article presents the characterization of THz wireless channel inside a metal box. We have found that both traveling wave and resonant modes exist inside the box. With the analysis of LoS propagation inside the metal box, it is found that the received power variation with respect to the antenna's height is due to the resonant modes dominated by first eight TE modes inside the metal box. The multipath introduced by traveling wave bouncing back and forth between the transceiver sides of the cavity limits the coherence bandwidths. Path loss model for LoS propagation inside the empty metal cavity have been conducted. For RNLoS propagation inside the metal box, it is found that traveling wave dominates the channel. Also, analysis show that the multipath introduced by parallel-plate structure has constructive effect to the channel; however, this constructive effect gradually decreases with the increase in ω, and it can be negligible when $\omega \geq 60\lambda$. Finally, by comparing the measurements performed in free space and inside the metal box, it is found that resonating modes inside the cavity can help reduce the mean path losses, but as combined with reflections of traveling wave, it also introduces stronger fluctuations over the observed frequency band.

REFERENCES

[1] S. Kim and A. Zajić, "Characterization of 300-GHz wireless channel on a computer motherboard," *IEEE Trans. Antennas Propag.*, vol. 64, no. 12, pp. 5411–5423, Dec. 2016.
[2] K. Banerjee, S. J. Souri, P. Kapur, and K. C. Saraswat, "3-D ICs: A novel chip design for improving deep-submicrometer interconnect performance and systems-on-chip integration," *Proc. IEEE*, vol. 89, no. 5, pp. 602–633, May 2001.
[3] D. A. B. Miller, "Rationale and challenges for optical interconnects to electronic chips," *Proc. IEEE*, vol. 88, no. 6, pp. 728–749, Jun. 2000.
[4] R. H. Havemann and J. A. Hutchby, "High-performance interconnects: An integration overview," *Proc. IEEE*, vol. 89, no. 5, pp. 586–601, May 2001.
[5] K. Kawasaki *et al.*, "A millimeter-wave intra-connect solution," *IEEE J. Solid-State Circuits*, vol. 45, no. 12, pp. 2655–2666, Dec. 2010.
[6] J. Branch, X. Guo, L. Gao, A. Sugavanam, J.-J. Lin, and K. K. O, "Wireless communication in a flip-chip package using integrated antennas on silicon substrates," *IEEE Electron Device Lett.*, vol. 26, no. 2, pp. 115–117, Feb. 2005.
[7] M. F. Chang, V. P. Roychowdhury, L. Zhang, H. Shin, and Y. Qian, "RF/wireless interconnect for inter- and intra-chip communications," *Proc. IEEE*, vol. 89, no. 4, pp. 456–466, Apr. 2001.
[8] K. Kim *et al.*, "The feasibility of on-chip interconnection using antennas," in *Proc. IEEE/ACM Int. Conf. Comput.-Aided Design*, 2005, pp. 979–984.
[9] S. Khademi, S. P. Chepuri, Z. Irahhauten, G. J. M. Janssen, and A.-J. van der Veen, "Channel measurements and modeling for a 60 GHz wireless link within a metal cabinet," *IEEE Trans. Wireless Commun.*, vol. 14, no. 9, pp. 5098–5110, Sep. 2015.
[10] J. Karedal, A. P. Singh, F. Tufvesson, and A. F. Molisch, "Characterization of a computer board-to-board ultra-wideband channel," *IEEE Commun. Lett.*, vol. 11, no. 6, pp. 468–470, Jun. 2007.
[11] Z. M. Chen and Y. P. Zhang, "Inter-chip wireless communication channel: Measurement, characterization, and modeling," *IEEE Trans. Antennas Propag.*, vol. 55, no. 3, pp. 978–986, Mar. 2007.

[12] D. W. Matolak, S. Kaya, and A. Kodi, "Channel modeling for wireless networks-on-chips," *IEEE Commun. Mag.*, vol. 51, no. 6, pp. 180–186, Jun. 2013.

[13] J. Gelabert, D. J. Edwards, and C. J. Stevens, "Experimental evaluation of UWB wireless communication within PC case," *Electron. Lett.*, vol. 47, no. 13, pp. 773–775, Jun. 2011.

[14] K. Ranachandran, R. Kokku, R. Mahindra, and S. Rangarajan, "60 GHz data-center networking: Wireless → worryless," NEC Lab. Amer., Princeton, NJ, USA, Tech. Rep. pp. 1–11.

[15] J.-Y. Shin, E. G. Sirer, H. Weatherspoon, and D. Kirovski, "On the feasibility of completely wirelesss datacenters," *IEEE/ACM Trans. Netw.*, vol. 21, no. 5, pp. 1666–1679, Oct. 2013.

[16] InifiBand. (2018). *Infiniband Roadmap*. [Online]. Available: https://www.infinibandta.org/infiniband-roadmap/

[17] P. C. Jain, "Recent trends in next generation terabit Ethernet and gigabit wireless local area network," in *Proc. Int. Conf. Signal Process. Commun. (ICSC)*, Dec. 2016, pp. 106–110.

[18] *IEEE Draft Standard for Information Technology—Telecommunications and Information Exchange Between Systems Local and Metropolitan Area Networks—Specific Requirements Part 11: Wireless LAN Medium Access Control (MAC) and Physical Layer (PHY) Specifications–Amendment: Enhanced Throughput for Operation in License-Exempt Bands Above 45 GHz*, Standard IEEE P802.11ay/D2.0, Jul. 2018, pp. 1–673.

[19] P. H. Siegel, "Terahertz technology," *IEEE Trans. Microw. Theory Techn.*, vol. 50, no. 3, pp. 910–928, Mar. 2002.

[20] R. Piesiewicz, T. Kleine-Ostmann, N. Krumbholz, D. Mittleman, M. Koch, and T. Kurner, "Terahertz characterisation of building materials," *Electron. Lett.*, vol. 41, no. 18, pp. 1002–1004, Sep. 2005.

[21] R. Piesiewicz, C. Jansen, D. Mittleman, T. Kleine-Ostmann, M. Koch, and T. Kürner, "Scattering analysis for the modeling of THz communication systems," *IEEE Trans. Antennas Propag.*, vol. 55, no. 11, pp. 3002–3009, Nov. 2007.

[22] C. Jansen, R. Piesiewicz, D. Mittleman, T. Kurner, and M. Koch, "The impact of reflections from stratified building materials on the wave propagation in future indoor terahertz communication systems," *IEEE Trans. Antennas Propag.*, vol. 56, no. 5, pp. 1413–1419, May 2008.

[23] J. M. Jornet and I. F. Akyildiz, "Channel modeling and capacity analysis for electromagnetic wireless nanonetworks in the terahertz band," *IEEE Trans. Wireless Commun.*, vol. 10, no. 10, pp. 3211–3221, Oct. 2011.

[24] C. Han, A. O. Bicen, and I. F. Akyildiz, "Multi-ray channel modeling and wideband characterization for wireless communications in the terahertz band," *IEEE Trans. Wireless Commun.*, vol. 14, no. 5, pp. 2402–2412, May 2015.

[25] S. Priebe and T. Kurner, "Stochastic modeling of THz indoor radio channels," *IEEE Trans. Wireless Commun.*, vol. 12, no. 9, pp. 4445–4455, Sep. 2013.

[26] A. F. Molisch, "Ultrawideband propagation channels-theory, measurement, and modeling," *IEEE Trans. Veh. Technol.*, vol. 54, no. 5, pp. 1528–1545, Sep. 2005.

[27] N. Khalid and O. B. Akan, "Wideband THz communication channel measurements for 5G indoor wireless networks," in *Proc. IEEE Int. Conf. Commun. (ICC)*, May 2016, pp. 1–6.

[28] S. Kim and A. G. Zajić, "Statistical characterization of 300-GHz propagation on a desktop," *IEEE Trans. Veh. Technol.*, vol. 64, no. 8, pp. 3330–3338, Aug. 2015.

[29] S. Priebe, C. Jastrow, M. Jacob, T. Kleine-Ostmann, T. Schrader, and T. Kurner, "Channel and propagation measurements at 300 GHz," *IEEE Trans. Antennas Propag.*, vol. 59, no. 5, pp. 1688–1698, May 2011.

[30] S. Priebe, M. Jacob, C. Jastrow, T. Kleine-Ostmann, T. Schrader, and T. Kurner, "A comparison of indoor channel measurements and ray tracing simulations at 300 GHz," in *Proc. 35th Int. Conf. Infr., Millim., THz. Waves*, Sep. 2010, pp. 1–2.

[31] M. Jacob, S. Priebe, R. Dickhoff, T. Kleine-Ostmann, T. Schrader, and T. Kurner, "Diffraction in mm and sub-mm wave indoor propagation channels," *IEEE Trans. Microw. Theory Techn.*, vol. 60, no. 3, pp. 833–844, Mar. 2012.

[32] T. Kürner, A. Fricke, S. Rey, P. Le Bars, A. Mounir, and T. Kleine-Ostmann, "Measurements and modeling of basic propagation characteristics for intra-device communications at 60 GHz and 300 GHz," *J. Infr., Millim., THz. Waves*, vol. 36, no. 2, pp. 144–158, 2015.

[33] J. Fu, P. Juyal, and A. Zajić, "300 GHz channel characterization of chip-to-chip communication in metal enclosure," in *Proc. 13th Eur. Conf. Antennas Propag. (EuCAP)*, Mar./Apr. 2019, pp. 1–5.

[34] H. T. Friis, "A note on a simple transmission formula," *Proc. IRE*, vol. 34, no. 5, pp. 254–256, May 1946.

[35] D. A. Hill, *Electromagnetic Fields in Cavities: Deterministic and Statistical Theories*, vol. 35. Wiley, 2009.

[36] A. Zajic, *Mobile-to-Mobile Wireless Channels*. Norwood, MA, USA: Artech House, 2013.

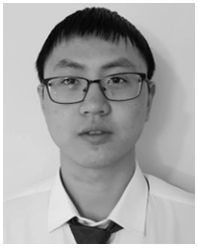

Jinbang Fu was born in Nanchang, China. He received the B.Sc. degree *(summa cum laude)* in electrical and computer engineering from the University of Massachusetts, Amherst, MA, USA, in 2017. He is currently pursuing the Ph.D. degree in electrical and computer engineering with the Georgia Institute of Technology, Atlanta, GA, USA.

He is a Graduate Research Assistant with the Electromagnetic Measurements in Communications and Computing Laboratory, Georgia Institute of Technology. His current research interests include terahertz (THz) wireless channel measurements and modeling, and THz wireless communication system design for chip-to-chip communication.

Prateek Juyal received the B.E. degree in electronics and communication engineering from Kumaun University, Nainital, India, in 2007, the M.Tech. degree in digital communication from Guru Gobind Singh Indraprastha University, Delhi, India, in 2009, and the Ph.D. degree in electrical and computer engineering from the University of Manitoba, Winnipeg, MB, Canada, in 2017.

He is currently a Post-Doctoral Fellow with the School of Electrical and Computer engineering, Georgia Institute of Technology, Atlanta, GA, USA. His current research interests include antenna design, metasurfaces application in radiating structures and terahertz (THz) wireless channel modeling, and propagation.

Alenka Zajić (S'99–M'09–SM'13) received the B.Sc. and M.Sc. degrees form the School of Electrical Engineering, University of Belgrade, Belgrade, Serbia, in 2001 and 2003, respectively, and the Ph.D. degree in electrical and computer engineering from the Georgia Institute of Technology, Atlanta, GA, USA, in 2008.

She was a Visiting Faculty Member with the School of Computer Science, Georgia Institute of Technology. She was a Post-Doctoral Fellow with the Naval Research Laboratory, Washington, DC, USA. She was a Design Engineer with Skyworks Solutions, Inc., Woburn, MA, USA. She is currently an Associate Professor with the School of Electrical and Computer Engineering, Georgia Institute of Technology. Her current research interests include electromagnetic, wireless communications, signal processing, and computer engineering.

Dr. Zajić was a recipient of the Best Student Paper Award at the 2007 Wireless Communications and Networking Conference, the Best Paper Award at the International Conference on Telecommunications in 2008, the 2012 Neal Shepherd Memorial Best Propagation Paper Award, the Best Student Paper Award at the IEEE International Conference on Communications and Electronics in 2014, the Best Paper Award at MICRO 2016, and the 2017 NSF CAREER Award. She received the Dan Noble Fellowship in 2004, which was awarded by Motorola, Inc. and the IEEE Vehicular Technology Society for quality impact in vehicular technology.